energies

Article

On the Design and Topology Selection of Permanent Magnet Synchronous Generators for Natural Impedance Matching in Small-Scale Uncontrolled Passive Wind Generator Systems

Casper J. J. Labuschagne * and Maarten J. Kamper

Department of Electrical and Electronic Engineering, Stellenbosch University, Stellenbosch 7600, South Africa; kamper@sun.ac.za
* Correspondence: 17539455@sun.ac.za

Abstract: Small-scale uncontrolled passive wind generator systems are an attractive solution for rural energy generation because of the system's reliability and low cost. However, designing these uncontrolled wind generators for good power matching with the wind turbine is challenging and often requires external impedance matching. In this paper, permanent magnet generators with different stator and rotor structures were investigated and designed to increase the generator's synchronous inductance for a natural impedance matching. For the design methodology, multi-objective optimisation was used to design the generators for near-maximum turbine power matching, whereby internal impedance matching was reached as much as possible. It was shown that altering the placement and orientation of the permanent magnets in the rotor is a viable method to achieve the desired impedance matching; however, these generators do not have the best performance. It was found that the surface-mounted permanent magnet generator with semi-closed slots was the optimum topology. An optimised generator prototype was tested for the experimental validation. All designs were verified by comparing the results of 2D and 3D finite-element analysis.

Keywords: design optimisation; impedance matching; passive wind generator system; permanent magnet synchronous generator; small-scale wind turbine; wind power generation

Citation: Labuschagne, C.J.J.; Kamper, M.J. On the Design and Topology Selection of Permanent Magnet Synchronous Generators for Natural Impedance Matching in Small-Scale Uncontrolled Passive Wind Generator Systems. *Energies* **2022**, *15*, 1888. https://doi.org/10.3390/en15051888

Academic Editor: Gerard-Andre Capolino

Received: 5 January 2022
Accepted: 25 February 2022
Published: 4 March 2022

1. Introduction

Energy generation for and the electrification of rural communities and farms are still some of the main socio-economic issues in developing countries. Especially for Sub-Sahara African countries, where it is estimated that a relatively small percentage of the rural population currently has access to electricity. In this context of rural energy generation and with the goal of climate change mitigation, distributed small-scale wind generator systems are an attractive option for independent AC or DC microgrids and can easily be deployed where there is no utility grid connection. However, reports have shown that these small-scale wind generator systems need to be more cost effective [1,2]; hence, there are currently incentives such as those outlined in [3] to make small-scale wind energy technology more cost competitive.

The small-scale uncontrolled passive wind generator system shown in Figure 1 is ideal for these rural applications. In Figure 1, only a diode bridge rectifier is used to directly connect the wind generator to the battery storage. Thus, the passive system uses minimal power electronics and is therefore conceivably more cost effective. The power electronics in small-scale wind energy systems are also the components most prone to failure [4,5]. The passive system in Figure 1 is therefore potentially more reliable, also reducing the operation and maintenance costs. The preferred generator technology for these small-scale systems is the permanent magnet synchronous generator (PMSG) [6]. However, because the system is uncontrolled, it is challenging to design the wind generator to have good power

matching with the wind turbine. Therefore, the focus in this paper was on designing PMSGs for these small-scale passive wind energy systems.

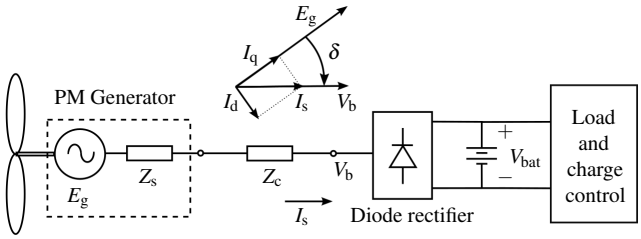

Figure 1. Single-line diagram of a passive wind energy system with an uncontrolled diode rectifier and battery storage.

Small-scale wind generator systems are deployed according to the need, and not necessarily at the optimum wind site, as in the case of utility-scale wind farms. Therefore, it is imperative that the wind generator matches well the available power from the wind turbine at lower wind speeds. Failure in this regard was highlighted by [7] as a major issue with current small-scale wind energy systems. Therefore, the design approach for the uncontrolled passive PMSGs, as in [8–10], where the wind generator was optimally designed according to a perceived "typical wind cycle", does not guarantee good power matching at low wind speeds and is not always considered ideal. In [11], the wind turbine's parameters were adjusted according to the generator to improve power matching. However, changing the wind turbine's parameters is not desirable. The challenge then, when designing these PMSGs, is to ensure good power matching with the wind turbine at lower wind speeds, as well as maximum power matching at the rated wind speed. It should also be noted that the PMSGs in [8–11] were all for power ratings lower than 1.5 kW.

In terms of the design optimisation strategy for the PMSGs, there are multiple approaches found in the literature. As already discussed, there are those in [8–11] for a passive system. In a more general sense, the recent reviews in [12,13] on optimisation trends for electric machines highlighted that the use of genetic algorithms for multi-objective design optimisation approaches is favourable for design problems with several performance measures. Moreover, multi-objective design optimisation is the most common approach for wind generator design, e.g., [14–17]. In [14–17], the actively controlled wind generators with maximum power point tracking (MPPT) were optimised for a specified drive-cycle to maximise annual energy production. However, as outlined in the previous paragraph, site-specific design is not necessarily the best option for small-scale uncontrolled wind generators. The generators in these small-scale uncontrolled passive wind energy systems must be designed to be geographically independent. Therefore, in this case, the main design problem is to match the wind generator's power with that of the wind turbine at lower wind speeds and at the specified rated operating point.

In [18], a method of external impedance matching was used to match the wind generator's power with the wind turbine, whereby an external inductance impedance was connected between the generator and the diode rectifier, shown in Figure 1. Although this method can be used effectively, as was done in [18,19], the additional external inductor is an unwanted component to the system. This incentivised the investigation performed in [20], which was to design PMSGs for a natural impedance matching the wind turbine, i.e., where the internal synchronous inductance of the PMSG alone was sufficient for good power matching. Hence, this paper is an extension of the work performed in [18,20] and forms part of an overarching study on PMSGs for passive wind generator systems.

In this paper, various methods of designing the PMSG to have an increased synchronous inductance for a natural impedance matching were investigated. These methods included altering the placement and orientation of the PMs in the rotor to change the magnetic saliency of the PMSG, as well as the stator slot's structure to increase leakage

flux. The various PMSG structures were designed for a sub-5 kW passive wind generator system, using a unique design methodology that ensured that the desired power matching with the wind turbine was achieved. The overall performance and cost effectiveness of the designed PMSGs were then evaluated to determine the optimal solution for this application. The results in this paper were validated with the experimental results of an optimally designed PMSG prototype.

2. Passive Wind Generator System

In this section, the wind generator specifications and equivalent circuit modelling are discussed. An analytical approximation for the impedance matching requirement is also given.

2.1. System Specifications

The wind turbine power versus turbine speed curves for a 4.2 kW passive wind generator system are shown in Figure 2. Shown also in Figure 2 is the maximum available turbine power that can be extracted from the wind (power curve *A*). Typically, generator operation along power curve *A* can be achieved by using an actively controlled synchronous rectifier in the system with MPPT. However, in the case of the uncontrolled passive system, the PMSG needs to be designed to match *naturally* the wind turbine power. Power curve *B*, in Figure 2, emulates power curve *A* at the cut-in speed and maximum rated power, showing the desired operation of the PMSG for the passive system. Thus, two operating points were specified for the PMSG's design, i.e., (i) the cut-in speed operating point, n_c, at which the PMSG starts supplying power to the battery storage and (ii) the rated speed operating point, n_r, where the rated power is generated. The cut-in and rated operating points are indicated in Figure 2, and the system's specifications are summarised in Table 1.

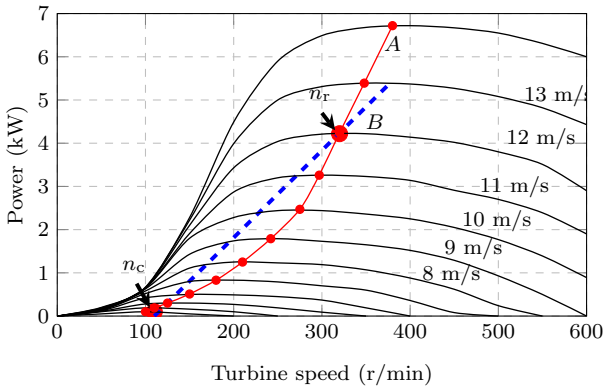

Figure 2. Wind turbine power versus speed curves, with wind generator impedance matching examples.

Table 1. Summary of specified operating points.

	n_c	n_r
Wind speed	3 m/s	12 m/s
Turbine speed	110 r/min	320 r/min
Generated power, P_g	0 kW	4.2 kW
Battery/DC grid voltage, V_b	48 V	

2.2. Wind Turbine

The wind turbine data in Figure 2 are for a horizontal axis wind turbine (HAWT). A schematic of the nacelle's assembly is shown in Figure 3. The wind turbine's blades and the PMSG were mounted off-centre in relation to the tower and tail vane, as shown in Figure 3b. Under extreme conditions, the wind pushes the turbine and generator out of the

wind and against the tail mechanism, which stays in line with the wind direction. In this way, the input power from the wind turbine is lowered, and system protection is provided. Furthermore, the HAWT's nacelle has an uncontrolled full degree of rotation and, therefore, requires brush slip rings for power transmission.

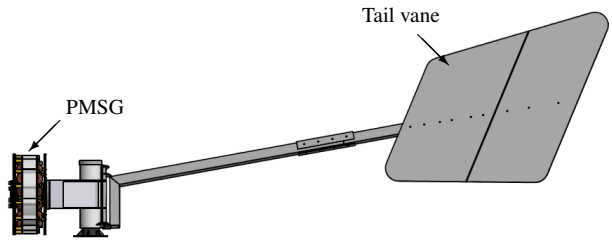

(**a**)

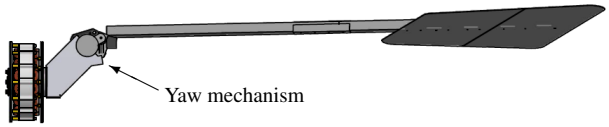

(**b**)

Figure 3. Schematic of the off-centre wind generator and tail vane assembly. (**a**) Side view. (**b**) Top view.

2.3. Impedance Matching

Because it is an uncontrolled passive system, the internal impedance of the PMSG, Z_s in Figure 1, needs to match correctly the battery storage (note that this is without external impedance matching). This then ensures that the PMSG's generated power matches the available wind turbine power at the rated operating point, n_r. Consider the following theoretical estimation of the necessary impedance:

The PMSG was modelled in the *dq*-reference frame. From the *dq*-equivalent circuits in Figure 4, the steady-state *dq*-equations in generator mode are:

$$\begin{aligned} V_q &= -R_{st}I_q - \omega_e L_d I_d + \omega_e \lambda_{PM} \\ &= -R_{st}I_q - \omega_e L_d I_d + E_g \\ V_d &= -R_{st}I_d + \omega_e L_q I_q. \end{aligned} \tag{1}$$

In Equation (1) and Figure 4, ω_e is the synchronous electrical speed, λ_{PM} is the PM flux linkage, E_g is the induced generator voltage, and R_{st} is the total per-phase resistance, which includes the PMSG's stator resistance, R_i, and the combined resistance of the brush slip rings and the resistance of the transmission cable, R_c. The phasor diagram for the passive system is shown in Figure 5a. In Figure 5a, the constrained terminal voltage, V_b, is the fixed fundamental per-phase voltage on the AC side of the diode rectifier. Due to the diode rectifier, the passive system will always operate at a unity displacement power factor [21], i.e., I_s and V_b are in phase.

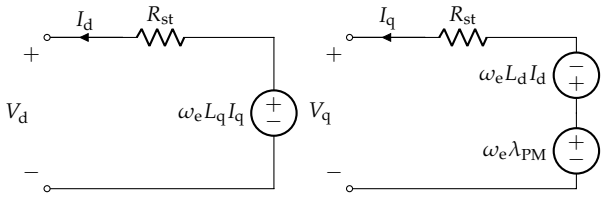

Figure 4. Per-phase *dq*-equivalent circuit diagram of the PMSG.

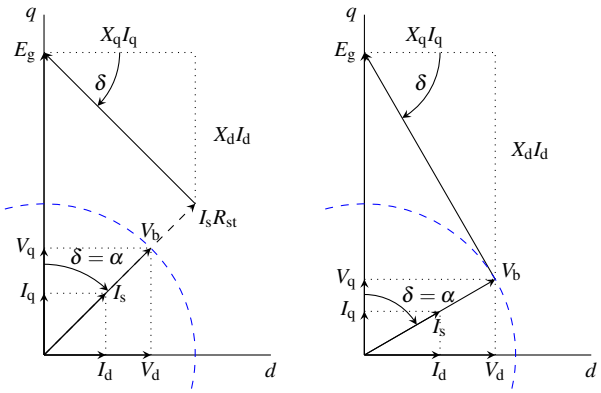

Figure 5. Passive system phasor diagrams.

For simplification, it was further assumed that R_{st} in (1) and Figure 5a is negligible. Therefore, we now have the phasor diagram in Figure 5b, and the voltage equations of (1) can be rewritten as:

$$\begin{aligned} V_q &= -\omega_e L_d I_d + E_g = -X_d I_d + E_g \\ V_d &= \omega_e L_q I_q = X_q I_q. \end{aligned} \tag{2}$$

At rated power, E_g can be calculated using:

$$E_g = aV_b \tag{3}$$

with:

$$a = \frac{n_r}{n_c} = \frac{320}{110} = 2.91. \tag{4}$$

From Figure 5b, we also have:

$$\cos(\delta) = \frac{V_b}{E_g} = \frac{1}{a} \Rightarrow \delta = \cos^{-1}\left(\frac{1}{a}\right) \tag{5}$$

and:

$$\tan(\delta) = \frac{V_d}{V_q} = \frac{I_d}{I_q} = \frac{X_d I_d}{X_q I_q} \Rightarrow \frac{X_d}{X_q} = 1.0. \tag{6}$$

Subsequently, by substituting a into (5) and then δ into (6), we have:

$$\frac{I_d}{I_q} = \tan(69.9^\circ) = 2.73 \tag{7}$$

with $V_b = I_s = 1.0$ pu, the per-unit values at rated power can be calculated and are summarised in Table 2.

Although R_{st} in Figure 5a cannot be ignored, the estimated per-unit results in Table 2 are remarkable in terms of how high the per-unit reactance must be to have the desired power matching. The required reactance at base speed is $X_d = X_q = 2.73/2.91 = 0.94$ pu, whereas surface-mounted PMSGs with non-overlapping windings have per-unit reactance values that are typically between 0.2 pu and 0.4 pu. Therefore, it is often necessary to add an external inductance, L_{ext}, between the PMSG and the diode rectifier [18]. With external impedance matching, the dq-equations in (1) are then:

$$\begin{aligned} V_q &= -R_{st} I_q - \omega_e (L_d + L_{ext}) I_d + \omega_e \lambda_{PM} \\ V_d &= -R_{st} I_d + \omega_e (L_q + L_{ext}) I_q. \end{aligned} \tag{8}$$

However, as explained before, the external inductance in the passive system is an undesired component. To eliminate the necessity of L_{ext}, careful consideration is needed when selecting the PMSG topology and the design of the PMSG in order to significantly increase the PMSG's impedance (reactance).

Table 2. Predicted PMSG *dq* values at rated power.

$P = 1.0$ pu	$V_b = 1.0$ pu	$I_s = 1.0$ pu	$E_g = 2.91$ pu
$V_d = 0.94$ pu		$I_d = 0.94$ pu	$X_d = 2.73$ pu
$V_q = 0.344$ pu		$I_q = 0.344$ pu	$X_q = 2.73$ pu

3. PMSG Topologies

3.1. Machine Selection

For small-scale wind generators, it is important that the generator has a low cogging torque. The wind turbine torque at the low cut-in wind speed (3 m/s) has to overcome this cogging torque for the generator to start generating power. A good indicator for predicting whether a PMSG will have a small no-load cogging torque is the least common multiple (LCM) between the number of stator slots, Q_s, and the number of poles, p. It generally holds true that the larger the value of the PMSG's LCM, the smaller the no-load cogging torque will be.

Seeing that the machine selection was for a low-speed direct-drive application, PMSGs with fractional-slot concentrated (non-overlapping) windings are very attractive [22]. Non-overlapping winding PMSGs (NO-PMSGs) have shorter end-winding lengths, resulting in less copper losses and a more compact mechanical structure [23]. Possible PMSG slot–pole combinations and their relevant characteristics are summarised in Table 3 for comparison. From Table 3, the best generator choice is the 30–28 PMSG. This particular combination has a good fundamental winding factor of $k_w \approx 0.951$ and a large LCM(Q_s, p) compared to the other slot–pole combinations.

Table 3. Comparison of potential slot–pole combinations for machines with fractional-slot concentrated windings.

Slot-Pole	**36–30 (6–5)**	**36–32 (9–8)**	**30–28 (15–14)**
LCM(Q_s, p)	180	288	420
k_w, working harmonic winding factor	0.933	0.945	0.951
τ_d, differential harmonic leakage flux coefficient	1.43	1.43	1.40

3.2. Stator Design

For the stator's structure, it is advantageous to have open slots with rectangular teeth, as shown in Figure 6a. This allows for preformed coils to be used, which are easier to manufacture. However, as shown in Section 2.3, it is desired to increase the PMSG's per phase synchronous inductance, L_s, for improved power matching. Therefore, alterations can be made to the stator structure in an attempt to increase L_s. Using rectangular semi-closed slots, as shown in Figure 6b, is one way to increase the PMSG's synchronous inductance:

The per-phase synchronous inductance can be calculated as:

$$L_s = L_m(1 + \tau_d) + L_{sl} + L_e, \quad (9)$$

where L_m is the magnetisation inductance, τ_d is the differential harmonic leakage flux coefficient, L_{sl} is the slot-leakage inductance, and L_e is the end-winding inductance. The magnetisation inductance is given by:

$$L_m = \frac{m(Wk_w)^2 d_i l_{Fe} \mu_0}{\pi p^2 g'_{air} K_s}, \tag{10}$$

where m is the number of phases, W is the number of turns in series per phase, k_w is the winding factor of the generator's working harmonic, d_i is the air gap diameter, l_{Fe} is the axial stack length, g'_{air} is the resultant air gap length taking Carter's factor into account, and K_s is the saturation factor.

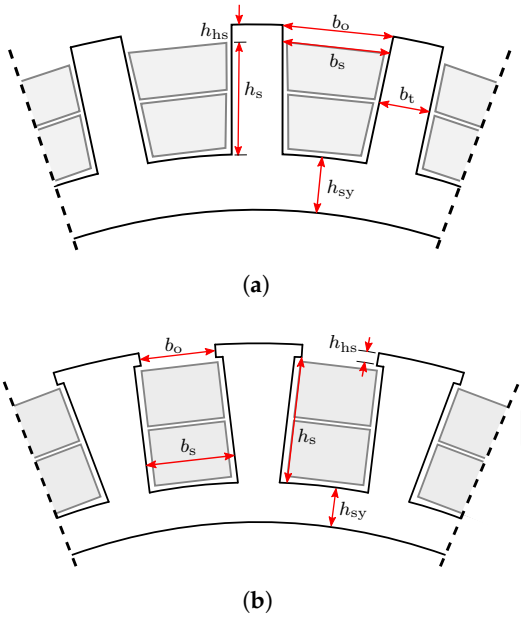

Figure 6. Stator slot structures and dimensions. (**a**) Open slot with rectangular teeth. (**b**) Semi-closed slot.

The slot-leakage inductance can be calculated as in [24,25], using:

$$L_{sl} = \frac{4m}{Q_s} \mu_0 l_{Fe} W^2 \lambda_{uv}. \tag{11}$$

Here, λ_{uv} is the slot permeance factor for a double-layer non-overlapping winding with a vertical coil side arrangement,

$$\lambda_{uv} \approx k_1 \frac{h_s}{3b_s} + k_2 \frac{h_{hs}}{b_o}. \tag{12}$$

In (12), k_1 and k_2 are given by:

$$\begin{aligned} k_1 &= 1 - \frac{3}{16} \frac{y_q - W}{q} \\ k_2 &= 1 - \frac{y_q - W}{4q} \end{aligned} \tag{13}$$

as in [24]. From (12) and the geometry definitions in Figure 6, it is shown theoretically that L_{sl}, and therefore L_s, can be increased by closing the stator slots and using a rectangular slot shape (λ_{uv} is inversely proportional to b_s and b_o). PMSGs with a semi-closed stator slot structure are therefore more likely to meet the desired impedance matching requirements.

The differential harmonic leakage flux coefficient in (9) is calculated from the harmonic analysis and is given by:

$$\tau_{\mathrm{d}} = \frac{\sum_{n \neq j} (\frac{k_{\mathrm{w}n}}{n})^2}{(\frac{k_{\mathrm{w}j}}{j})^2}. \tag{14}$$

The τ_{d} values for the different slot–pole PMSGs are given in Table 3. Typically, PMSGs with non-overlapping windings have much larger τ_{d} values than PMSGs with overlapping windings, which is another reason for using non-overlapping winding PMSGs for passive wind generator systems.

3.3. Rotor Design

In terms of the PM rotor structure, it is possible to increase the synchronous inductance by altering the placement and the orientation of the PMs in the rotor, thus effectively "building" the necessary external inductance into the PMSG. In [20], this was shown to be a valid approach for designing PMSGs to have a natural impedance matching in a passive wind generator system. The different rotor structures considered in this investigation are shown in Figure 7. Figure 7a shows the surface-mounted PM (S-PM) rotor; Figure 7b shows the embedded PM (E-PM) rotor; Figure 7c the interior-spoke-type PM (SP-PM) rotor. As a result of using interior PM rotors, there is a significant increase in stator magnetisation flux compared to that of an S-PM rotor. This also results in a larger difference between the direct-axis and quadrature-axis inductances of the machine (also referred to as the magnetic saliency) [25]. Typical machine saliency properties for the different rotor topologies in Figure 7 are summarised in Table 4.

Table 4. Typical saliency properties of different rotor structures and relative slot-leakage inductance of different stator slot openings.

Rotor Structure	**Saliency, ξ**	**Stator Structure**	**L_{sl}**
Surface-mounted PM	$L_{\mathrm{q}} \approx L_{\mathrm{d}}$	Open slot	Smaller L_{sl}
Interior embedded PM	$L_{\mathrm{q}} > L_{\mathrm{d}}$	Semi-closed slot	Larger L_{sl}
Interior-spoke-type PM	$L_{\mathrm{q}} > L_{\mathrm{d}}$		

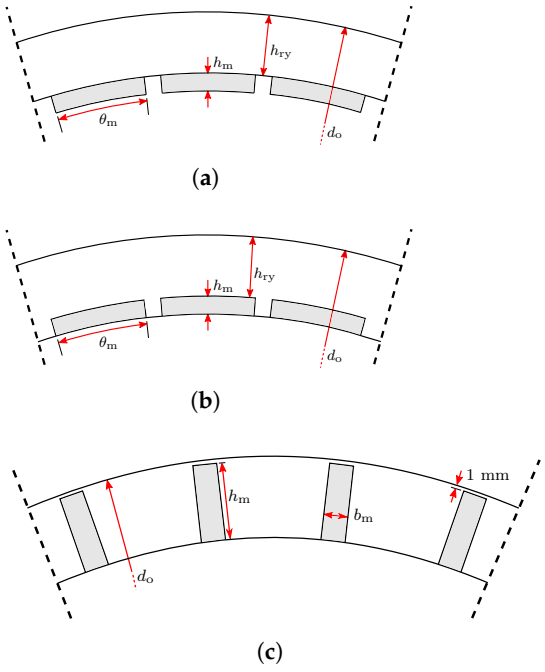

Figure 7. Rotor structures and dimensions. (**a**) Surface-mounted PM rotor; (**b**) embedded PM rotor; (**c**) interior PM spoke-type rotor.

Opting to use either surface (S-PM) or interior PM (E-PM and SP-PM) rotor structures has certain tradeoffs when it comes to manufacturing and machine performance. In the case of an S-PMSG, the PMs are exposed, whereas for the interior PM rotors, the PMs are protected and at a low risk of being damaged. Embedding the PMs in the rotor also has the additional advantage that the PMs are well protected against demagnetisation. It is also apparent from Figure 7 that the S-PMSG is more likely to use less iron material than the E-PMSG and SP-PMSG. The latter is an important design aspect, considering the need for a low top-tower mass.

Designing the SP-PMSG rotor as the one in [26] could reduce the active mass; however, it could also compromise the structural integrity of the PMSG. For the structural integrity of the SP-PM rotor in Figure 7c, the yoke needs support on at least one side of the interior embedded PM. It is shown in Figure 8 that the support section on the rotor yoke adds an additional path for stray leakage flux from the PMs. Shown also in Figure 8, there is a large component of leakage flux to the exterior air region of the rotor. The effect of the outer air region was not taken into account in [20], and it was later found to have a significant effect on the SP-PMSG's performance and the outcome of the comparison.

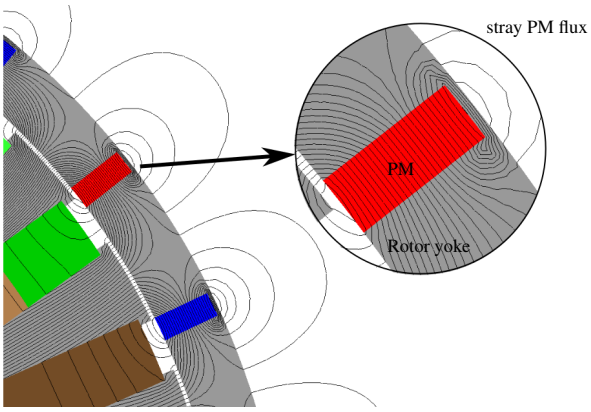

Figure 8. Enlarged section of an SP-PMSG, showing the PM flux paths and leakage flux in the rotor.

4. Design and Optimisation

In this section, the design approach and methodology for the different PMSG topologies outlined in Section 3 is discussed. The PMSG topologies then were the S-PMSG, E-PMSG, and SP-PMSG with open slots and the S-PMSG, E-PMSG, and SP-PMSG with semi-closed rectangular slots.

With iron-cored PMSGs, it is difficult to accurately take saturation and armature reaction into account, even more so in this case, with the PMSG operating with a large direct-axis current, as shown in Figures 1 and 5. In [10], an analytical model was used to design the PMSG for a passive wind generator system; however, substantial errors of 17% and 26% were reported for the generated torque and back-EMF. Furthermore, in [18], it was also shown that using analytical calculations for the synchronous inductance resulted in a significant error in power matching with the wind turbine. The results in [10,18] confirmed that it is better to use finite-element analysis (FEA) for PMSGs in passive wind generator systems. Therefore, the performance of the PMSGs in this paper was solved using 2D static FEA. End-effects were taken into account in the 2D FEA for the respective PMSGs, as in [27,28].

4.1. Multi-Objective Optimisation

The population-based non-gradient genetic algorithm II (NSGA-II) [29] was used in conjunction with the 2D static FEA solutions to optimise the PMSGs. The design optimisation workflow is shown in Figure 9.

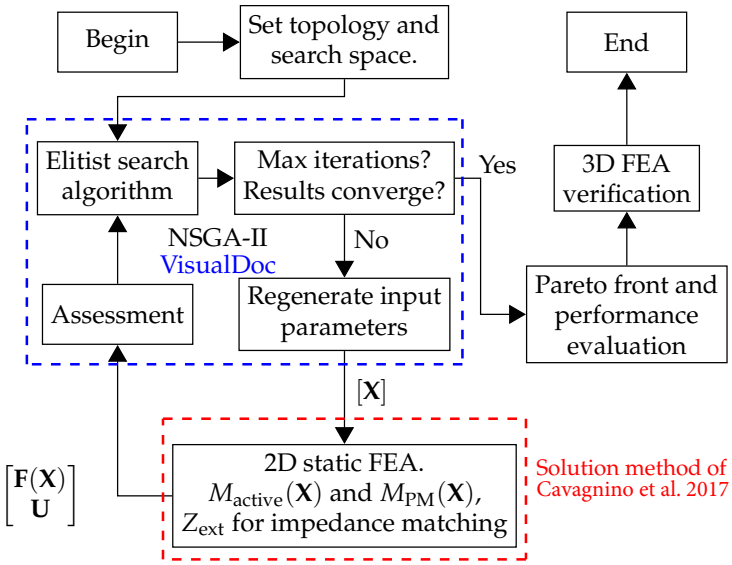

Figure 9. Design and optimisation flow diagram [12].

Reducing the PMSG's cost and minimizing the top-tower mass are important for small-scale wind generators. Therefore, the first two objectives of the multi-objective function given in (15) were to minimise the PMSG's active mass, M_{active}, and the generator's PM mass, M_{PM}. Minimizing M_{active} has the dual purpose of reducing the generator's cost and the top-tower mass. The generator's PM mass, M_{PM}, is the most expensive material and, given its volatile cost, needs to be minimised as a separate objective.

$$\min_{\mathbf{X}} \ \mathbf{F}(\mathbf{X}) = \min_{\mathbf{X}} \begin{bmatrix} M_{active}(\mathbf{X}) \\ M_{PM}(\mathbf{X}) \\ Z_{ext}(\mathbf{X}) \end{bmatrix}. \tag{15}$$

The PMSG's active mass in (15) is calculated as:

$$M_{active} = M_{Fe} + M_{PM} + M_{Cu}, \tag{16}$$

where M_{Fe} is the collective mass of the stator and rotor iron laminations and M_{Cu} is the total copper winding mass, which includes the end-winding mass.

The other objective in (15) is to minimise the impedance error, Z_{ext}. This is the required difference in generator impedance, if not zero, to match the generator's power with the turbine at the rated operating point, as shown in Figure 10a. The impedance error is visually illustrated in Figure 10b as a physical external impedance component ($Z_{ext} = j\omega_e L_{ext}$), which is added, if necessary, to the passive generator system between the generator and the diode bridge rectifier. As shown in Figure 9, the impedance error is calculated with the solution method for external impedance matching given in [18]. The impedance error is then given as feedback to the optimisation algorithm. In this way, the optimisation algorithm finds non-dominated PMSG solutions where $Z_{ext} = 0$, i.e., where the PMSGs are designed for the correct synchronous impedance Z_s that matches *naturally* the maximum wind turbine power, or alternatively, where the PMSGs match the wind turbine power with the correct external impedance added to the system.

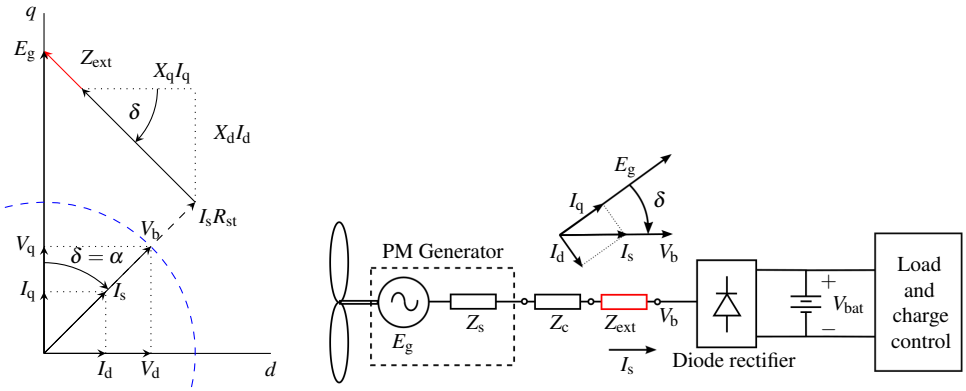

Figure 10. (**a**) Passive system phasor diagram with external impedance matching, Z_{ext}. (**b**) Single-line diagram of the PM wind generator with external inductance for impedance matching connected in the passive wind turbine system. The optimisation (15) accordingly minimises Z_{ext} to zero if possible.

4.2. Design Constraints and Input Parameters

The design constraints for the PMSGs at the rated operating point are given by:

$$\mathbf{U} = \begin{bmatrix} P_g \\ \eta \\ J_{rms} \end{bmatrix} = \begin{bmatrix} 4.2\ \text{kW} \\ \geq 90\% \\ \leq 5\ \text{A/mm}^2 \end{bmatrix}. \tag{17}$$

In (17), P_g is the rated power, η is the generator efficiency, and J_{rms} is the maximum allowed RMS current density. The constraint on P_g was imposed to ensure that the desired power matching was achieved between the PMSG and the wind turbine. The constraint on J_{rms} is a thermal constraint and is a typical value for small-scale machines of this power rating [25].

In (15), **X** is the input vector generated by NSGA-II containing the relevant dimensions for each topology, as defined in Figures 6 and 7. A parameterised geometry was used to maintain a realistic optimisation search space, and four geometric boundaries were imposed: the outer diameter was limited to that of the wind turbine's nacelle $d_o < 400$ mm; the relevant rotor and stator yoke heights had to be h_{ry}, $h_{sy} > 6$ mm to maintain structural integrity; as a precaution for demagnetisation and for manufacturing ease (brittle PMs) of the S-PMSG, the minimum allowed PM height was $h_m > 3$ mm. For all the PMSG designs, the mechanical air gap was kept constant at $g_{air} = 1$ mm. For the SP-PMSGs, the rotor yoke support, as shown in Figure 7c, was kept constant at 1 mm. For the PM material, NdFeB N48 was used.

5. FEA Results and Evaluation

5.1. Optimisation Results

The multi-objective optimisation Pareto front results are shown in Figure 11. The Pareto fronts in Figure 11 show the tradeoff between M_{active} and M_{PM} and provide insight into how the different PMSG topologies compare with one another. For the third objective in (15), to minimise Z_{ext}, the PMSG solutions where $Z_{ext} = 0$ are also indicated in Figure 11. For these solutions, the internal impedance of the PMSG was sufficient for near-maximum power matching. It is shown in Figure 11a that, for the S-PMSG with open stator slots, none of the solutions met the desired *natural* impedance matching and required an external inductance for good power matching. Moreover, the Pareto front results in Figure 11 confirmed that altering the stator slot and rotor structure to increase L_{sl} and the magnetic saliency, ξ, were both viable methods to increase L_s for a natural impedance matching. For the 3D Pareto front plots, refer to Figure A1 in Appendix A.

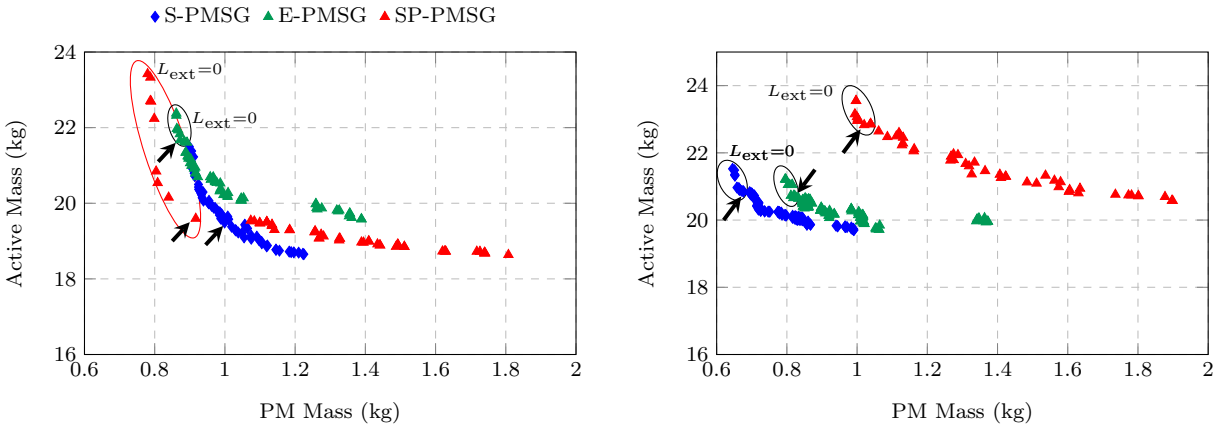

(**a**) (**b**)

Figure 11. Multi-objective optimisation Pareto front results. (**a**) Open slots; (**b**) semi-closed slots.

For each PMSG topology, the optimum design was selected at the optimal tradeoff between the design objectives, as indicated in Figure 11. The performance results are summarised in Table 5. Although the efficiency values in Table 5 were slightly lower than specified, they were still deemed acceptable. Altogether, the results in Table 5 confirmed that the performance constraints in (17) were met. In terms of M_{active} and M_{PM}, the SP-PMSG with open slots and the S-PMSG with semi-closed slots were the best options. This is also evident from the Pareto fronts shown in Figure 11. However, the difference between these two PMSG topologies was not that significant. The S-PMSG with open slots was also competitive in terms of M_{active} and M_{PM}. However, this topology can be discarded due to the necessary external inductance. The dimensions of the optimum PMSGs in Table 5 are given in Table A1 in Appendix A.

5.2. Power Matching

To illustrate the natural impedance matching of the respective PMSGs in Table 5, the FEA predicted power curves are plotted against the wind turbine's power curves in Figure 12. The PMSGs start generating power at the specified cut-in speed and achieve good power matching at low wind speeds, which is essential for this application. The respective PMSGs also match the wind turbine at the rated operating speed. Overall, the power matching plots in Figure 12 are desirable, with the respective E-PMSGs and SP-PMSGs, as well as the S-PMSG with semi-closed slots matching naturally the wind turbine. To show that the generators maintain a high efficiency over a wide range of speeds and torques, the semi-closed slot S-PMSG's FEA predicted output power, P_{out}, is plotted in Figure 12b.

5.3. Torque Quality

Good torque quality is essential for small-scale wind generators, specifically the generator's cogging torque, since the wind turbine has to overcome this to start generating power. The cogging torque, ΔT_{cog}, and rated torque ripple, ΔT_{r}, results for the respective PMSGs in Table 5 are summarised in Table 6. All of the PMSGs had a very low cogging torque, with $\Delta T_{\text{cog}} < 2.1\%$ for all of the PMSGs. However, the torque ripple results for the interior embedded PMSG topologies in Table 6 are undesired ($\Delta T_{\text{r}} > 10\%$). For comparison, the FE predicted ΔT_{cog} and ΔT_{r} for the semi-closed rectangular slot S-PMSG and the open slot SP-PMSG are shown for the mechanical rotation of one rotor pole pair (360 electrical degrees) in Figure 13.

Table 5. Comparison of selected Pareto front PMSG solutions.

Open Slot	S-PMSG	E-PMSG	SP-PMSG
M_{PM} (kg)	1.0	0.87	0.92
M_{active} (kg)	19.49	21.67	19.60
Z_{ext} (Ω)	0.36	0	0
P_g (kW)	4.18	4.17	4.12
η (%)	89.1	89.8	89.8
J (A/mm^2)	5.0	4.93	4.97
T_g (Nm)	124.9	124.3	122.8
L_q (mH)	2.71	3.90	3.43
L_d (mH)	2.58	2.94	3.00
ξ	1.05	1.33	1.14
X_s (pu)	1.6	2.48	2.28
d_o (mm)	376	375	383
l_{Fe} (mm)	40	47	36.2
Semi-closed slot	S-PMSG	E-PMSG	SP-PMSG
M_{PM} (kg)	0.72	0.82	0.99
M_{active} (kg)	21.33	20.72	23.15
Z_{ext} (Ω)	0	0	0
P_g (kW)	4.26	4.10	4.10
η (%)	89.8	89.9	89.8
J (A/mm^2)	5.0	5.0	4.9
T_g (Nm)	127.1	122.2	122.4
L_q (mH)	3.12	4.25	3.95
L_d (mH)	2.95	3.01	2.69
ξ	1.06	1.41	1.41
X_s (pu)	1.95	2.52	2.37
d_o (mm)	376	376	384
l_{Fe} (mm)	49	48	42

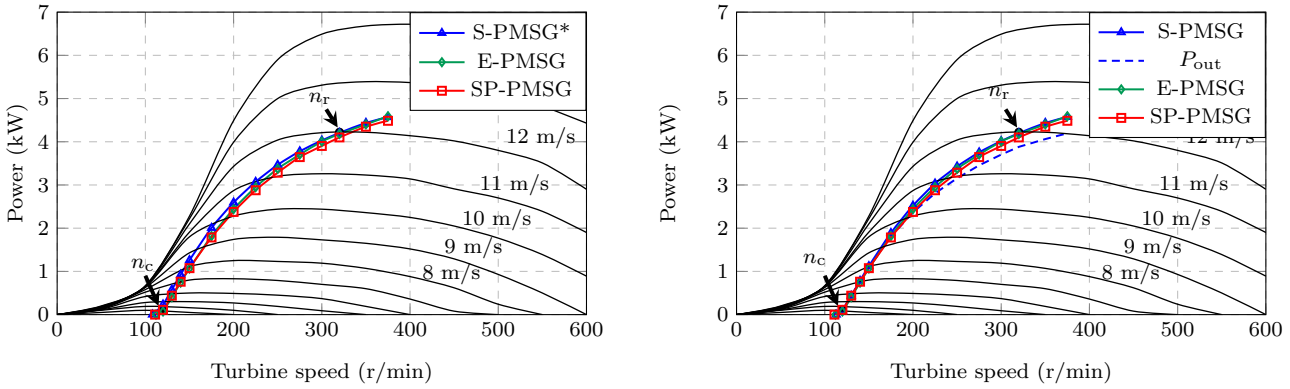

(**a**) (**b**)

Figure 12. Power curves of the selected PMSGs in Table 5. (**a**) Open slots; (**b**) semi-closed slots.

Table 6. Comparison of PMSG torque quality.

Open slot	S-PMSG	E-PMSG	ST-PMSG
ΔT_{cog}, (%)	1.2	1.2	2.0
ΔT_r, (%)	6.6	12.4	12.5
Semi-closed slot	S-PMSG	E-PMSG	ST-PMSG
ΔT_{cog}, (%)	1.5	1.9	2.1
ΔT_r, (%)	4.9	13.0	17.1

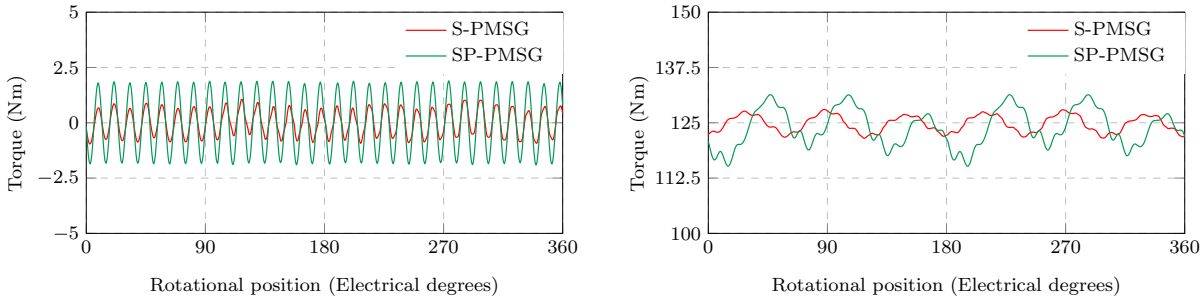

Figure 13. FE-predicted cogging torque and torque ripple of the S-PMSG with semi-closed slots and the SP-PMSG with open slots in Table 5. (**a**) Cogging torque, ΔT_{cog}; (**b**) torque ripple, ΔT_r.

5.4. Demagnetisation

Irreversible demagnetisation in small-scale PM wind generators can occur during short-circuit fault conditions or at high PM temperatures. Furthermore, at the full-load rated operating point, the PM generator in an uncontrolled passive wind generator system will operate with a relatively large *d*-axis current. This causes a strong magnetic field that opposes that of the PMs, which in turn may cause demagnetisation to occur. The geometric constraint on h_m in the design optimisation was imposed to reduce the risk of demagnetisation. Regardless, the PMSG designs in Table 5 still need to be evaluated for irreversible demagnetisation to determine the risk thereof.

It is evident from the power curves in Figure 12 that the power in the passive wind generator system was limited independent of the wind speed. Therefore, PM demagnetisation in the PMSGs was analysed at the generator's rated speed, n_r (thus at rated load). The demagnetisation prediction plots for the two S-PM rotor topologies are shown in Figure 14a,b respectively. It is shown in Figure 14a that, for the open-slot S-PMSG, demagnetisation will start occurring at PM temperatures > 50 °C. However, the temperature of the PMs during operation are not expected to surpass 50 °C. In Figure 14b, it is shown that the PMs in the semi-closed slot S-PMSG were at very low risk of demagnetizing, with demagnetisation only occurring at >80° (this was later confirmed with thermal measurements that are given in Figure A3 in Appendix B). Similarly, for the embedded interior E-PMSG and SP-PMSG topologies, it was found that the PMSGs were at low risk of demagnetizing, with slight demagnetisation only starting to occur at PM temperatures >80 °C.

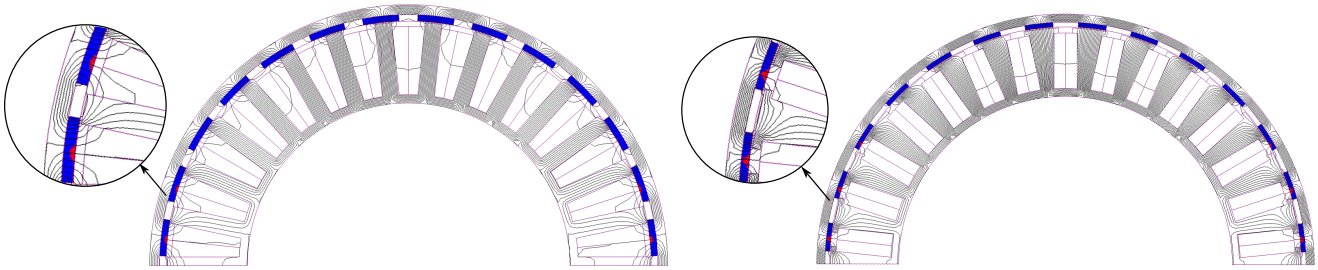

Figure 14. Demagnetisation prediction at different temperatures (indicated by red colour in the magnets) for the S-PMSGs in Table 5 at rated conditions (320 r/min and full load), using NdFeB N48. (**a**) S-PMSG open slots, 50 °C PM temperature; (**b**) S-PMSG semi-closed slots, 80 °C PM temperature.

5.5. Three-Dimensional FEA Performance Validation

To validate the 2D FEA solutions and optimisation results, the performance of the respective PMSGs in Table 5 were also solved using 3D FEA. The 3D models of the semi-

closed slot S-PMSG and the open-slot SP-PMSG are shown in Figure 15a,b, respectively. The 2D versus 3D FEA results are summarised in Table 7.

It is shown in Table 7 that the 3D-FEA-generated torque, T_g, and generator efficiency, η, at rated speed n_r correlated well with the 2D FEA results. Given also in Table 7 are the calculated iron losses, P_{Fe}, at both n_r and n_c. The iron losses at n_c are important because the wind turbine needs to overcome the PMSG's open-circuit losses (predominantly P_{Fe}) up to the cut-in speed, n_c, to start generating power. It is shown in Table 7 that the 2D and 3D FEA core losses at n_c compared well. For the interior embedded PMSG topologies, the 2D-FEA-calculated core losses at n_r were lower than the 3D-FEA-calculated core losses. However, the effect on the PMSGs' performance at n_r is shown to be minor.

Table 7. Comparison of 2D versus 3D FEA PMSG performance.

Open slot	S-PMSG		E-PMSG		SP-PMSG	
	2D	3D	2D	3D	2D	3D
T_g (Nm)	124.9	128.8	124.3	131.6	122.8	113.7
η (%)	89.1	89.4	89.8	90.0	89.8	88.7
P_{Fe} at n_r (W)	25.1	28.5	21.9	37.5	20.7	31.8
P_{Fe} at n_c (W)	10.7	12.6	10.0	12.3	11.4	10.5
Semi-closed slot	S-PMSG		E-PMSG		SP-PMSG	
	2D	3D	2D	3D	2D	3D
T_g (Nm)	127.1	126.7	122.2	118.9	122.4	115.4
η (%)	89.8	89.9	89.8	89.2	89.8	89.0
P_{Fe} at n_r (W)	31.3	33.9	29.4	49.8	26.5	35.0
P_{Fe} at n_c (W)	13.9	12.5	12.4	13.7	11.6	11.8

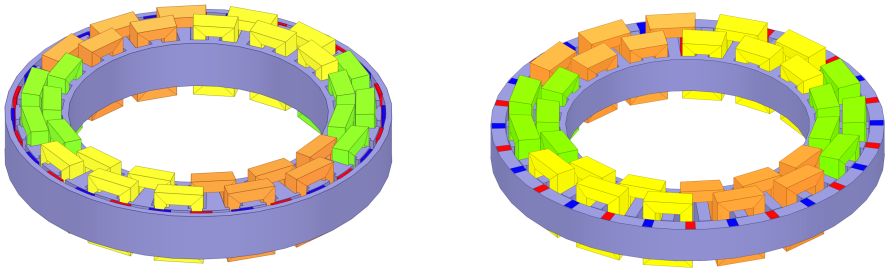

(**a**) (**b**)

Figure 15. Three-dimensional FEA models for some of the PMSGs in Table 5. (**a**) S-PMSG, semi-closed slots; (**b**) SP-PMSG, open slots.

5.6. Discussion

Considering all aspects of the performance evaluation performed in the previous subsections, it is evident that the S-PMSG with semi-closed slots is the best generator topology. The results in Table 5 indicate that this PMSG is competitive in terms of active material costs and the generator's active mass. Furthermore, this PMSG has good power matching with the wind turbine, achieving the desired natural impedance matching, as well as having superior torque quality.

6. Prototype and Experimental Validation

For the experimental validation, a prototype of the S-PMSG with semi-closed slots in Table 5 was built. The manufactured prototype is shown in Figure 16a. It is shown in Figure 16b that the axial overhang of the end-winding length, l_g, was larger than what was designed. In the 2D FEA, this length was taken as $l_g = 5$ mm; however, the actual

measured value was $l_g = 20$ mm (This is an error by the winder. It is possible to wind the machine for the designed overhang length.). For the experimental validation, this length was taken into account in the FEA solutions.

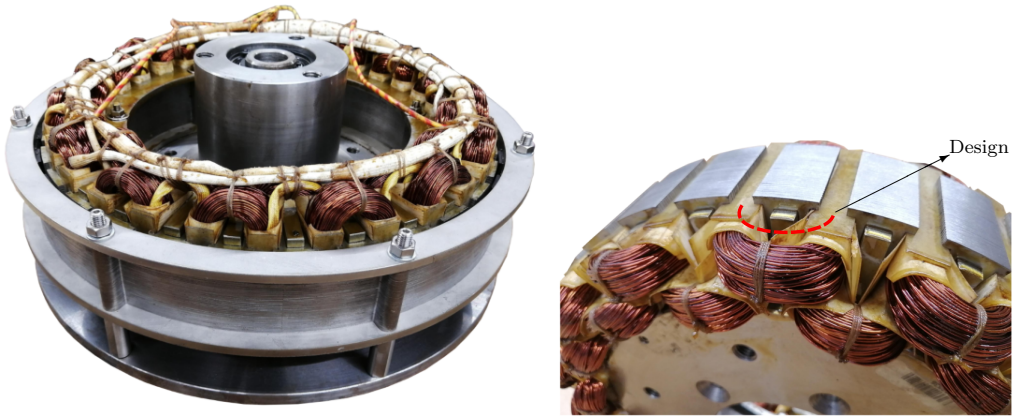

(**a**) (**b**)

Figure 16. S-PMSG prototype with semi-closed slots. (**a**) PMSG; (**b**) design versus actual end-winding overhang length.

The experimental setup on the test bench is shown in Figure 17. In Figure 17, the S-PMSG prototype was mechanically connected to a geared induction motor drive that emulated the wind turbine. The torque sensor in Figure 17 was used to measure the input power. The S-PMSG prototype was electrically connected to the battery bank via a diode bridge rectifier. The 48 V battery bank energy storage and discharge load are also shown in Figure 17.

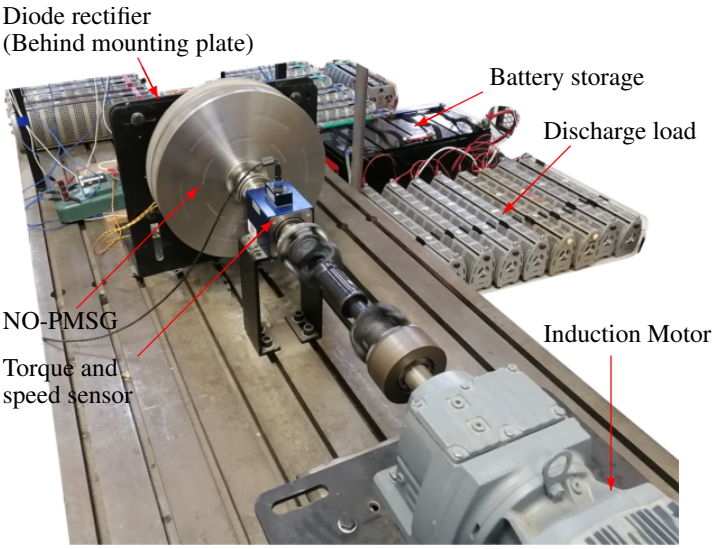

Figure 17. Experimental test bench setup of the manufactured PMSG prototype.

6.1. Power Matching Measurements

The measured results for the S-PMSG prototype's generated power, P_g, and output power, P_{out}, are shown in Figure 18. It is shown that the P_g power measurements were much lower than what was designed (green FEA curve). The following explanation accounts for the measured results in Figure 18.

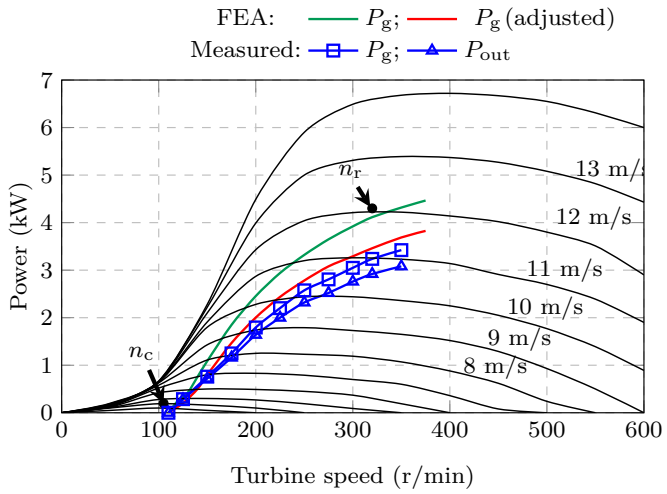

Figure 18. Measured power matching results of the S-PMSG prototype.

The manufacturer of the prototype's PMs could only guarantee certain dimensional tolerances on the PMs. Initially, these tolerances were considered insignificant. However, Figure 19 shows that the S-PMSG's performance was very sensitive to these manufacturing tolerances, i.e., the magnet height h_m and the magnet pitch angle θ_m. It is shown in Figure 19 that the PMSG's generated torque was particularly sensitive to h_m, seeing as a smaller magnet height also results in a larger air gap. Attempts to measure the height and width of the PMs with a digital calliper are shown in Figure A2 in Appendix B. In Figure A2a,b, it is shown that the average PM height was $h_m \approx 3.1$ mm, instead of the $h_m = 3.3$ mm for which the PMs were designed. Shown also in Figure A2c,d is that the magnet pitch angle and PM length were also slightly below the designed values.

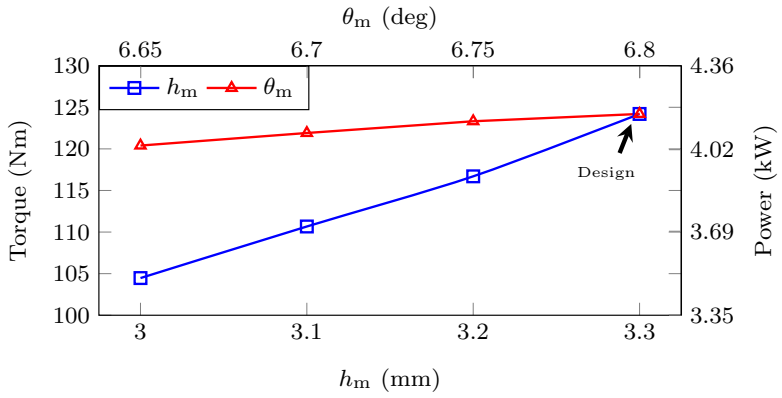

Figure 19. Effect of PM manufacturing tolerances on the generated torque and power at $n_r = 320$ r/min.

It is shown in Figure 18 that, if the PMs' dimensions were adjusted in the FEA accordingly, a better correlation between the measured power matching and the FEA (red curve) predicted power matching would be obtained. The measured and FEA results are also summarised in Table 8. The adjusted 2D and 3D FEA results are both included in Table 8. The deviation between the measured and 2D FEA predicted P_g in Table 8 at $n_r = 320$ r/min was 5%. All measurements were taken at steady-state temperature. The thermal measurements are given in Figure A3 in Appendix B.

Table 8. Summary of C-PMVG prototype measurements.

	FEA (Adjusted)		Measured
	2D	**3D**	
Parameters			
- PM height, h_m (mm)	3.1		3.1
- PM angle, θ_m (deg)	6.75		6.75
- PM length, l_{Fe} (mm)	48.35		48.35
- Phase resistance, R_s (Ω)	0.133	0.133	0.130
- Synchronous inductance, L_s (mH)	3.23	3.46	3.48
Performance at $n_r = 320$ r/min			
- P_g (kW)	3.43	3.46	3.26
- η (%)	89.3	88.6	86.5
P_{rot} (W)			118
P_{Cu} (W)			337
- E_g (V)	61.4	60.6	60.9

The measured current and voltage waveforms are shown in Figure 20. The current waveform in Figure 20 are sinusoidal and also correctly 30 deg out of phase with the fundamental line voltage, i.e., the PMSG was operating at a unity displacement power factor.

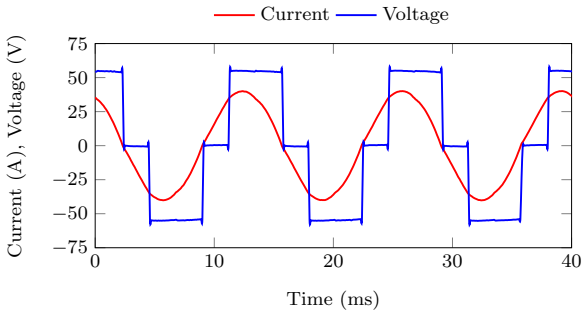

Figure 20. Measured phase current and line voltage at $n_r = 320$ r/min, showing the operation at a unity displacement power factor.

6.2. No-Load and Short-Circuit Measurements

The no-load open-circuit voltage measurements versus FEA-calculated voltage are shown in Figure 21. The values for the measured no-load open circuit voltage at $n_r = 320$ r/min are also summarised in Table 8. The measured versus FEA results in Figure 21 showed a good correlation. This verified the results in the previous subsection and the effect of the manufacturing tolerances of the PMs.

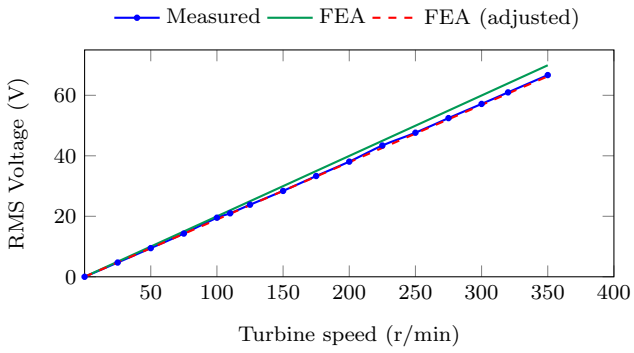

Figure 21. Measured open-circuit voltage versus FEA-calculated voltage.

The measured no-load rotational losses are also plotted in Figure 22 and are compared to the no-load 2D FEA-predicted iron losses P_{Fe}. The difference can be attributed to wind and friction losses that were not accounted for in the design process. These additional wind and friction losses then also accounted for a portion of the 5% difference between the measured and FEA-predicted P_g in Figure 18 and Table 8, as well as the difference in efficiency η. The measured rotational losses at n_r and rated load were 118 W. As shown in the no-load measurements in Figure 18, wind and friction losses accounted for approximately half of this. the latter indicates that the iron losses P_{Fe} at rated load were slightly higher than what was predicted in the FEA solutions and would account for the lower efficiency measurement in Table 8.

The internal synchronous inductance was measured by means of a number of short-circuit tests to obtain an average value. It is shown in Table 8 that the average measured L_s was very close to the FEA calculated values.

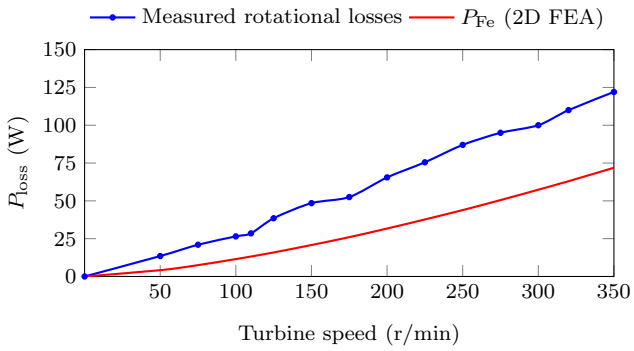

Figure 22. Measured no-load open-circuit losses versus no-load FEA-calculated iron losses.

7. Conclusions

In this paper, different topology PMSGs were considered in the design process of wind generators for small-scale uncontrolled passive wind generator systems. This was performed to investigate whether the resulting higher internal impedance of the generator, from either using an interior PM rotor or a different stator slot structure, was sufficient to achieve the desired power matching with the wind turbine. The respective PMSGs were designed using a multi-objective design optimisation approach. The following main conclusions were drawn from the investigation:

For PMSGs with surface-mounted PMs on the rotor, it was shown that the required impedance for a natural impedance matching with the wind turbine could be attained by changing the stator structure. Using semi-closed slots, as opposed to open slots, was shown to be a better design choice. Using semi-closed slots reduced the risk of PM demagnetisation and did not compromise the generator's torque quality. The S-PMSG with semi-closed slots was also the most cost-effective generator and, therefore, ultimately, the optimal generator choice.

Altering the rotor structure and the orientation of the PMs in the rotor to increase the magnetic saliency was shown to be another viable method to achieve the desired impedance matching. However, in this case, it was clear that an open-slot stator structure should be used. The E-PMSG and SP-PMSG topologies also had poor torque quality compared to the S-PMSG generators. Therefore, it is not recommended that these topologies be used for small-scale wind generators. Careful attention should also be paid to the leakage and end-effects of SP-PMSGs, as these can have a significant impact on the generator's performance if ignored.

The results presented in this paper were validated by a good comparison between the calculated and measured results of a prototype S-PMSG with semi-closed stator slots. However, it was shown that, when the PM material was minimised to the extreme in the design optimisation, the manufacturing tolerances on the PMs could have a significant effect on the power matching results. This was a very important outcome, showing that

manufacturing tolerances should be accounted for more rigorously in the design process and manufacturing, especially in relation to PM height.

Author Contributions: Conceptualisation, C.J.J.L. and M.J.K.; methodology, C.J.J.L. and M.J.K.; software, C.J.J.L.; validation, C.J.J.L.; formal analysis, C.J.J.L.; investigation, C.J.J.L.; resources, M.J.K.; data Curation, C.J.J.L.; writing—original draft preparation, C.J.J.L.; writing—review and editing, C.J.J.L. and M.J.K.; visualisation, C.J.J.L.; supervision, M.J.K.; project administration, M.J.K.; funding acquisition, M.J.K. All authors have read and agreed to the published version of the manuscript.

Funding: This research was funded by the Centre for Renewable and Sustainable Energy Studies (CRSES) at Stellenbosch University, South Africa, and the Department of Science and Innovation (DSI) in South Africa.

Acknowledgments: The authors would like to acknowledge K. Cloete and A. W. Labuschagne for their help with the mechanical drawings for the prototype. Thanks also to the workshop staff at the Department of Electrical and Electronic Engineering, Stellenbosch University, for their help with the prototype's assembly and manufacturing.

Conflicts of Interest: The authors declare no conflict of interest.

Abbreviations

The following abbreviations are used in this manuscript:

FEA	Finite-element analysis
HAWT	Horizontal axis wind turbine
LCM	Least common multiple
NO-PMSG	Non-overlapping winding permanent magnet synchronous generator
NSGA-II	Non-dominated sorting genetic algorithm II
PMSG	Permanent magnet synchronous generator
S-PM	Surface-mounted permanent magnet
E-PM	Embedded interior permanent magnet
SP-PM	Spoke-type interior permanent magnet

Appendix A. Additional Design Detail

The 3D Pareto front results are shown in Figure A1. The boundaries and optimal values of the decision variables in the optimisation are summarised in Table A1.

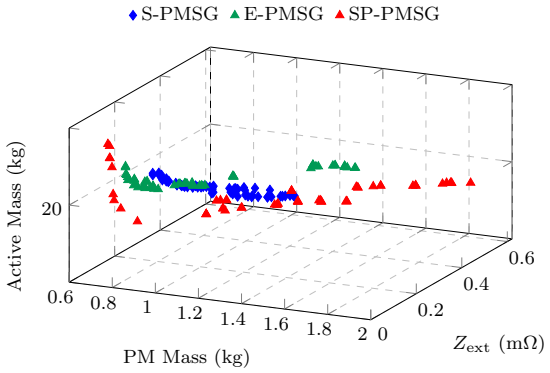

(**a**) Open slots

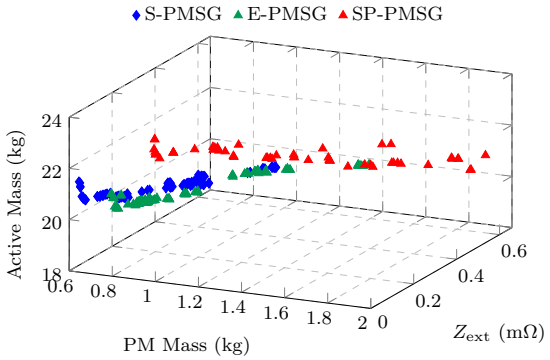

(**b**) Semi-closed slots

Figure A1. Multi-objective optimisation Pareto front results of all three objectives.

Table A1. Decision variables of the optimal selected PMSGs in Table 5.

Open slot	Boundaries	S-PMSG	E-PMSG	SP-PMSG
d_o (mm)	$d_o \leq 400$	375.5	374.7	382.9
h_{yr} (mm)	$6 \geq h_{yr} \leq 20$	7.1	7.0	1.0
h_m (mm)	$3 \geq h_m \leq 10$	4.5	3.0	-
h_m (mm)	$3 \geq h_m \leq 30$	-	-	13.3
θ_m (deg)	[c] $0.5 \geq \theta_m \leq 0.9$	8.5	9.3	-
b_m (mm)	[c] $0.05 \geq b_m \leq 0.5$	-	-	9.1
h_{hs} (mm)	$3 \geq h_{hs} \leq 10$	3.0	3.0	3.0
h_s (mm)	$10 \geq h_s \leq 75$	49.1	43.3	48.5
b_t (mm)	[a] $0.1 \geq b_t \leq 0.7$	12.2	12.8	11.6
h_{ys} (mm)	$6 \geq h_{ys} \leq 20$	6.1	7.1	6.0
l_{Fe} (mm)	$20 \geq l_{Fe} \leq 200$	40.0	47.4	36.2
Semi-closed slot	Boundaries	S-PMSG	E-PMSG	SP-PMSG
d_o (mm)	$d_o \leq 400$	375.6	376.3	384.3
h_{yr} (mm)	$6 \geq h_{yr} \leq 20$	6.2	7.4	1.0
h_m (mm)	$3 \geq h_m \leq 10$	3.3	3.0	-
h_m (mm)	$3 \geq h_m \leq 30$	-	-	12.6
θ_m (deg)	[c] $0.5 \geq \theta_m \leq 0.9$	6.8	8.8	-
b_m (mm)	[c] $0.05 \geq b_m \leq 0.5$	-	-	8.8
h_{hs} (mm)	$3 \geq h_{hs} \leq 10$	3.8	3.1	3.1
h_s (mm)	$10 \geq h_s \leq 75$	41.5	37.3	47.7
b_o (mm)	[b] $0.5 \geq b_o \leq 1.0$	10.5	12.7	15.9
b_s (mm)	[a] $0.3 \geq b_s \leq 0.9$	17.5	19.4	16.9
h_{ys} (mm)	$6 \geq h_{ys} \leq 20$	6.0	6.1	7.7
l_{Fe} (mm)	$20 \geq l_{Fe} \leq 200$	48.5	47.6	42.4

Boundaries are imposed in terms of the [a] slot pitch, [b] slot opening pitch, or [c] pole pitch.

Appendix B. Supplementary Measurements

Appendix B.1. PM Dimensions

Figure A2 shows the attempted measurements of the actual PM dimensions using a digital calliper. Figure A2a,b is for different PMs to show that the average value was taken.

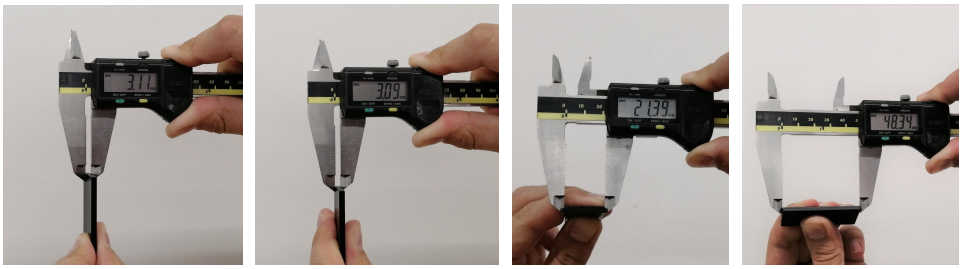

(**a**) (**b**) (**c**) (**d**)

Figure A2. Measuring the PM dimensions. (**a**) $h_m = 3.11$ mm; (**b**) $h_m = 3.09$ mm; (**c**) $\theta_m < 6.8$ deg; (**d**) $l_{Fe} < 48.5$ mm.

Appendix B.2. Thermal Measurements

The thermal measurements are shown in Figure A3. The thermal measurements confirmed that indirect cooling through self-ventilation would be effective and that the PMs were at low risk of demagnetizing.

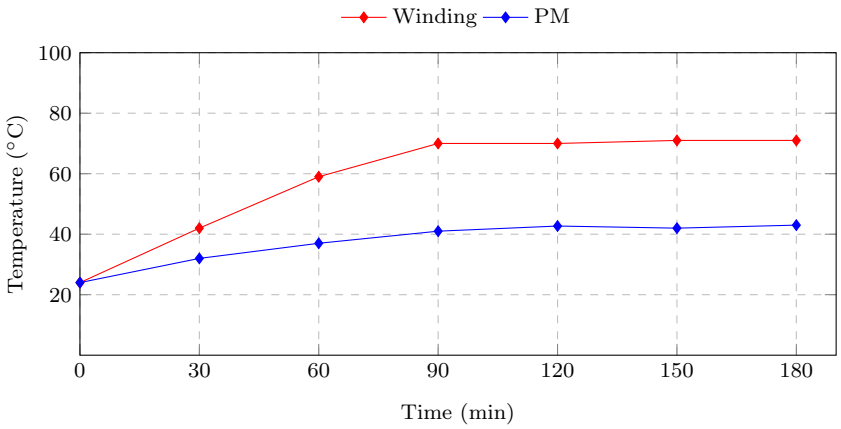

Figure A3. Temperature measurements while performing the load tests at rated speed n_r.

References

1. Hermanus, L.; Scholtz, L. *Small-Scale Renewable Energy Technologies in East Africa: An Overview*; Technical Report; WWF South Africa: Cape Town, South Africa, 2018.
2. Fitzgerald, D.; Terblanche, U. *Potential East African Localisation of Small-Scale Renewable Energy Manufacture*; Technical Report; Centre for Renewable and Sustainable Energy Studies (CRSES): Stellenbosch, South Africa, 2020.
3. Orrell, A.C.; Kazimierczuk, K.; Sheridan, L. *Distributed Wind Market Report*, 2021st ed.; Technical Report; Pacific Northwest National Laboratory (PNNL): Richland, WA, USA, 2021.
4. Carroll, J.; McDonald, A.; McMillan, D. Reliability Comparison of Wind Turbines With DFIG and PMG Drive Trains. *IEEE Trans. Energy Convers.* **2015**, *30*, 663–670. [CrossRef]
5. Arifujjaman, M.; Iqbal, M.T.; Quaicoe, J.E. Reliability analysis of grid connected small wind turbine power electronics. *Appl. Energy* **2009**, *86*, 1617–1623. [CrossRef]
6. Alnasir, Z.; Kazerani, M. An analytical literature review of stand-alone wind energy conversion systems from generator viewpoint. *Renew. Sustain. Energy Rev.* **2013**, *28*, 597–615. [CrossRef]
7. Ani, S.O.; Polinder, H.; Ferreira, J.A. Comparison of Energy Yield of Small Wind Turbines in Low Wind Speed Areas. *IEEE Trans. Sustain. Energy* **2013**, *4*, 42–49. [CrossRef]
8. Sareni, B.; Abdelli, A.; Roboam, X.; Tran, D. Model simplification and optimization of a passive wind turbine generator. *Renew. Energy* **2009**, *34*, 2640–2650. [CrossRef]

9. Tran, D.H.; Sareni, B.; Roboam, X.; Espanet, C. Integrated Optimal Design of a Passive Wind Turbine System: An Experimental Validation. *IEEE Trans. Sustain. Energy* **2010**, *1*, 48–56. [CrossRef]
10. Agrebi, H.Z.; Benhadj, N.; Chaieb, M.; Sher, F.; Amami, R.; Neji, R.; Mansfield, N. Integrated Optimal Design of Permanent Magnet Synchronous Generator for Smart Wind Turbine Using Genetic Algorithm. *Energies* **2021**, *14*, 4642. [CrossRef]
11. Aredjodoun, J.G.; Chetangny, P.K.; Houndedako, S.; Vianou, A.; Chamagne, D.; Espanet, C. Optimal adaptation of the wind rotor to the permanent magnets synchronous generator of a small passive wind turbine. In Proceedings of the 2019 IEEE PES/IAS PowerAfrica, Abuja, Nigeria, 20–23 August 2019; pp. 164–169.
12. Cavagnino, A.; Bramerdorfer, G.; Tapia, J.A. Optimization of electric machine Designs-Part II. *IEEE Trans. Ind. Electron.* **2017**, *65*, 1700–1703. [CrossRef]
13. Bramerdorfer, G.; Tapia, J.A.; Pyrhönen, J.J.; Cavagnino, A. Modern electrical machine design optimization: Techniques, trends, and best practices. *IEEE Trans. Ind. Electron.* **2018**, *65*, 7672–7684. [CrossRef]
14. Jung, S.Y.; Jung, H.; Hahn, S.C.; Jung, H.K.; Lee, C.G. Optimal Design of Direct-Driven PM Wind Generator for Maximum Annual Energy Production. *IEEE Trans. Magn.* **2008**, *44*, 1062–1065. [CrossRef]
15. Isfahani, A.H.; Boroujerdi, A.H.S.; Hasanzadeh, S. Multi-objective design optimization of a large-scale directdrive permanent magnet generator for wind energy conversion systems. *Front. Energy* **2014**, *8*, 182–191. [CrossRef]
16. Bazzo, T.; Kolzer, J.; Carlson, R.; Wurtz, F.; Gerbaud, L. Multidisciplinary design optimization of direct-drive PMSG considering the site wind profile. *Electr. Power Syst. Res.* **2016**, *141*, 467–475. [CrossRef]
17. Dmitrievskii, V.; Prakht, V.; Kazakbaev, V. Design optimization of a permanent-magnet flux-switching generator for direct-drive wind turbines. *Energies* **2019**, *12*, 3636. [CrossRef]
18. Labuschagne, C.J.J.; Kamper, M.J. Wind Generator Impedance Matching in Small-Scale Passive Wind Energy Systems. *IEEE Access* **2021**, *9*, 22558–22568. [CrossRef]
19. Stegmann, J.A.; Kamper, M.J. Design Aspects of Double-Sided Rotor Radial Flux Air-Cored Permanent-Magnet Wind Generator. *IEEE Trans. Ind. Appl.* **2011**, *47*, 767–778. [CrossRef]
20. Labuschagne, C.J.J.; Kamper, M.J. Evaluation of PM Rotor Topologies for Impedance Matching of Small-Scale Passive DC-Connected Wind Generator Systems. In Proceedings of the 2020 International Conference on Electrical Machines (ICEM), Gothenburg, Sweden, 23–26 August 2020; Volume 1, pp. 1896–1902. [CrossRef]
21. Mohan, N.; Undeland, T.M.; Robbins, W.P. *Power Electronics: Converters, Applications, and Design*; John Wiley & Sons: Hoboken, NJ, USA, 2003.
22. Chen, H.; Zuo, Y.; Chau, K.T.; Zhao, W.; Lee, C.H.T. Modern electric machines and drives for wind power generation: A review of opportunities and challenges. *IET Renew. Power Gener.* **2021**, *15*, 1864–1887. [CrossRef]
23. EL-Refaie, A.M. Fractional-Slot Concentrated-Windings Synchronous Permanent Magnet Machines: Opportunities and Challenges. *IEEE Trans. Ind. Electron.* **2010**, *57*, 107–121. [CrossRef]
24. Madariaga, C.; Jara, W.; Tapia, J.A.; Pyrhönen, J.; Lindh, P.; Riedemann, J.A. Closed-Form Solution for the Slot Leakage Inductance of Tooth-Coil-Winding Permanent Magnet Machines. *IEEE Trans. Energy Convers.* **2019**, *34*, 1572–1580. [CrossRef]
25. Pyrhonen, J.; Jokinen, T.; Hrabovcova, V. *Design of Rotating Electrical Machines*; John Wiley & Sons: West Sussex, UK, 2013.
26. Chirca, M.; Oprea, C.; Teodosescu, P.D.; Breban, S. Optimal design of a radial flux spoke-type interior rotor permanent magnet generator for micro-wind turbine applications. In Proceedings of the 2016 International Conference on Applied and Theoretical Electricity (ICATE), Craiova, Romania , 6–8 October 2016; pp. 1–5. [CrossRef]
27. Potgieter, J.H.J.; Kamper, M.J. Calculation Methods and Effects of End-Winding Inductance and Permanent-Magnet End Flux on Performance Prediction of Nonoverlap Winding Permanent-Magnet Machines. *IEEE Trans. Ind. Appl.* **2014**, *50*, 2458–2466. [CrossRef]
28. Volpe, G.; Marignetti, F.; Roggia, S.; Popescu, M.; Goss, J. Modified 2-D Model for 3-D Rotor Magnet Leakage Effects in PM Spoke Machines. *IEEE Trans. Ind. Appl.* **2019**, *55*, 3087–3096. [CrossRef]
29. Deb, K.; Pratap, A.; Agarwal, S.; Meyarivan, T. A fast and elitist multiobjective genetic algorithm: NSGA-II. *IEEE Trans. Evol. Comput.* **2002**, *6*, 182–197. [CrossRef]